NANO LETTERS

pubs.acs.org/NanoLett Letter

Extreme In-Plane Thermal Conductivity Anisotropy in Titanium Trisulfide Caused by Heat-Carrying Optical Phonons

Huili Liu,[#] Xiaoxia Yu,[#] Kedi Wu, Yang Gao, Sefaattin Tongay, Ali Javey, Lidong Chen,* Jiawang Hong,* and Junqiao Wu*

Cite This: *Nano Lett.* 2020, 20, 5221−5227 Read Online

ACCESS | Metrics & More | Article Recommendations | Supporting Information

ABSTRACT: High in-plane anisotropies arise in layered materials with large structural difference along different in-plane directions. We report an extreme case in layered TiS_3, which features tightly bonded atomic chains along the *b*-axis direction, held together by weaker, interchain bonding along the *a*-axis direction. Experiments show thermal conductivity along the chain twice as high as between the chain, an in-plane anisotropy higher than any other layered materials measured to date. We found that in contrast to most other materials, optical phonons in TiS_3 conduct an unusually high portion of heat (up to 66% along the *b*-axis direction). The large dispersiveness of optical phonons along the chains, contrasted to many fewer dispersive optical phonons perpendicular to the chains, is the primary reason for the observed high anisotropy in thermal conductivity. The finding discovers materials with unusual thermal conduction mechanism, as well as provides new material platforms for potential heat-routing or heat-managing devices.

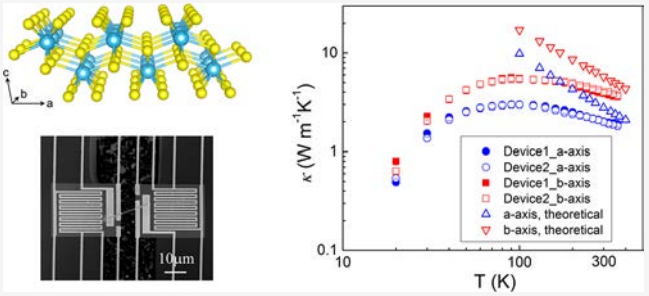

KEYWORDS: *Titanium trisulfide, in-plane anisotropy, optical phonons, thermal conductivity*

Layered materials are held together between layers via weak, van der Waals (vdW) interactions, whereas within each layer the atoms are bonded together by much stronger covalent bonding. They draw tremendous research attention by their fascinating physical properties as a new class of two-dimensional (2D) materials when thinned down to the monolayer. Potential applications of these materials are being investigated for fields ranging from electronics,[1−3] catalysis,[4] and photonics[5,6] to sensing[7,8] and thermoelectrics.[9] Not surprisingly, the weak interlayer vdW interactions combined with the strong intralayer covalent bonding may lead to high anisotropies in properties between the cross-plane and in-plane directions. Additionally, it has also been realized that there exists structural anisotropy within the basal plane of most layered materials, such as the difference in armchair (AC) and zigzag (ZZ) structures in black phosphorus (b-P),[10,11] black arsenic (b-As),[12] tin selenide (SnSe),[13] and graphene.[14] This would result in modest in-plane anisotropies in physical properties, offering potential applications that are not possible with isotropic materials.[15]

Recently, layered transition metal trichalcogenides (TMTCs), MX_3 (M = Zr, Ti, and X = S, Se), have become a focus of interest,[16,17] attributed mostly to their unique, quasi-one-dimensional (1D) chain structure in the basal plane.[18,19] Among them, titanium trisulfide (TiS_3) has a direct bandgap of ∼1.0 eV,[20,21] and a high on/off ratio of ∼7000 when made into field effect transistors.[22] Experiments show distinct carrier mobility of 80 and 40 $cm^2\ V^{-1}\ s^{-1}$ along its *b*- and *a*-axis directions, respectively,[23] and an unusual sulfur−sulfur lone-pair vibrational mode of TiS_3.[24] However, an important physical property, thermal conductivity (κ), has not been experimentally characterized in TiS_3, especially related to its unique quasi-1D chain structure in the basal plane. In this work, we report an extreme in-plane anisotropy in κ of TiS_3 up to a ratio of 2, higher than any currently known layered materials, by combining advanced thermal transport measurements with first-principles calculations.

TiS_3 takes a monoclinic structure with the space group of $P2_1/m$ (a = 4.96 Å, b = 3.40 Å, c = 8.79 Å, $\alpha = \gamma = 90°$, β = 97.3°).[25] Figure 1a shows a schematic of the crystal structure of a single layer. Importantly, the basal plane features one-dimensional atomic chains along the *b*-axis direction, as shown in Figure 1b. The bonding lengths in the chain are 2.45 and 2.49 Å,[26] slightly smaller than the sum of the individual covalent radii (1.05 and 1.60 Å for S and Ti,[27] respectively). The neighboring chains are laterally connected by longer Ti−S bonds along the *a*-axis, as shown in Figure 1c. These interchain

Received: April 8, 2020
Revised: June 15, 2020
Published: June 15, 2020

https://dx.doi.org/10.1021/acs.nanolett.0c01476
Nano Lett. 2020, 20, 5221−5227

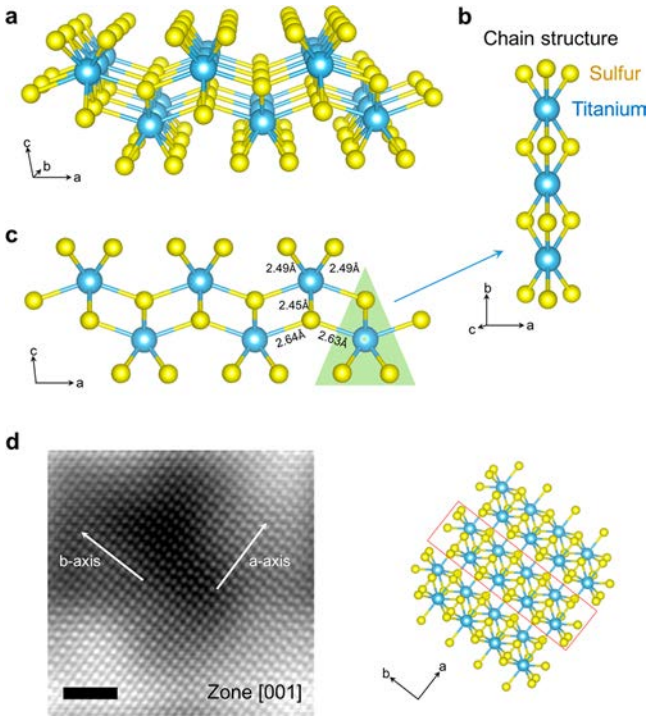

Figure 1. Crystal structure of TiS_3. (a) Monolayer of TiS_3. (b) Chain structure along the *b*-axis. (c) Side view of the monolayer. (d) TEM micrograph imaged along the *c*-axis (left) and the corresponding schematic structure (right). The red box indicates the chain along the *b*-axis. Scale bar, 1 nm.

bonding lengths are 2.63 and 2.64 Å, respectively, nearly equal to the sum of the individual covalent radii. This unique chain structure leads to high electronic, structural and vibrational anisotropies in the basal plane of TiS_3. For the electronic structure, the $3p_x$ orbitals of S atoms contribute mostly to the top of the valence band, which dominates the band dispersion along the *a*-axis direction; the $3d_{x^2-y^2}$ orbitals of Ti atoms compose the conduction band, dispersing mostly along the *b*-axis direction.[28] Figure 1d is a high-resolution TEM (transmission electron microscopy) image of TiS_3, showing atomic arrangement along the *a*- and *b*-axis, consistent with the chain structures seen in the right panel.

Figure 2a shows a TiS_3 flake mechanically exfoliated from the bulk crystal, where the crystallographic orientations were confirmed by micro-Raman analysis, as the Raman signal intensity depends on the angle between the laser polarization direction and the TiS_3 crystal orientation.[17] Raman intensity of the most prominent peak[17] (372 cm^{-1}) was fitted by theoretical angular dependence, $I \propto \cos^2 \varphi$, shown as a solid curve in Figure 2b, where $\varphi = 0°$ (90°) corresponds to the $a(b)$-axis direction of TiS_3. Details of device fabrication and measurements are in the Supporting Information.[10,11] Figure 2c shows a set of *a*-axis-oriented TiS_3 nanoribbons of length ~40 μm and width varying from 0.5 to 2 μm, e-beam lithographically patterned from a single flake with a thickness of 100 nm. The electrical contact of devices is improved by Pt deposition, as shown in Figure 2d,e, which results in negligible contact thermal resistance (Figure 2f) for the devices. All measurements were performed under high vacuum ($<10^{-6}$ Torr) with a radiation shield.[29−31] The flexible and suspended nature of the device maximally releases any tensile, shearing, and torsional stress potentially built up in the nanoribbon, as well as eliminates substrate influence, during the measurements.

Figure 3a shows the temperature dependence of κ measured along the *a*- (defined as κ_a) and *b*-axis (κ_b) directions. It is found that κ_b is much higher than κ_a near room temperature,

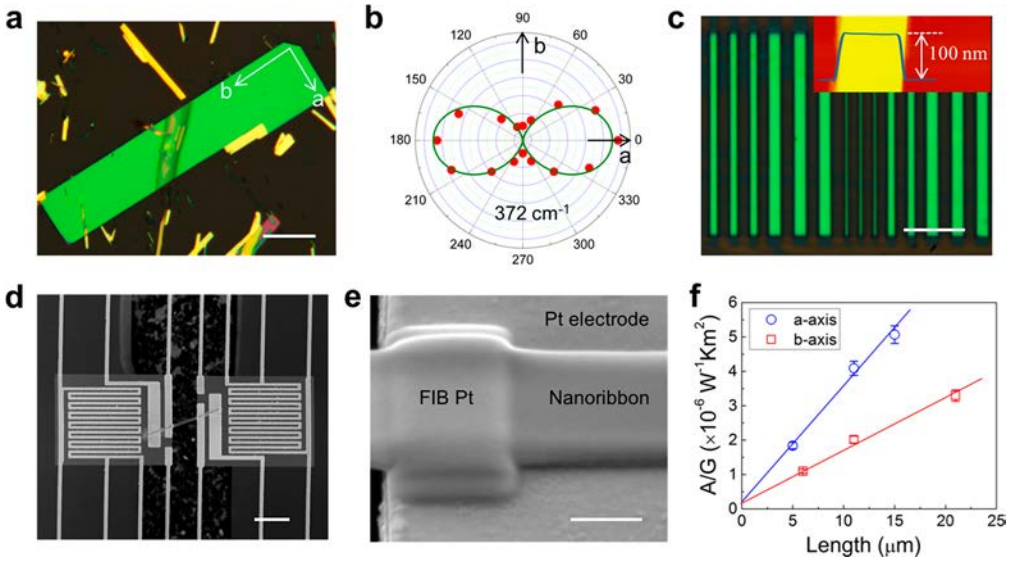

Figure 2. TiS_3 device fabrication for thermal and electrical measurements. (a) Optical image of exfoliated TiS_3 flakes. (b) Angular dependence of the intensity of the A_g Raman mode at 372 cm^{-1}. Solid curve is fitting to determine the crystal orientation along the *a*-axis and *b*-axis. (c) Optical image of lithographically patterned TiS_3 nanoribbons. Inset is an AFM (atomic force microscopy) image that shows the thickness of 100 nm (error bar, 3 nm). (d) SEM (scanning electron microscopy) image of a suspended micropad device supporting a single nanoribbon. (e) SEM image of part of the nanoribbon Pt-bonded onto the underlying electrode by FIB (Focused Ion Beam). (f) Cross-sectional area/thermal conductance (A/G) as a function of the nanoribbon length. Error bars include those from data of thermal conductance and sample size. These nanoribbons were made from the same flake (100 nm thick). The linear relation extrapolating to nearly zero indicates negligible thermal contact resistance for the measured nanoribbons devices. Scale bars: 50 μm (a); 10 μm (c), (d); 500 nm (e).

https://dx.doi.org/10.1021/acs.nanolett.0c01476
Nano Lett. 2020, 20, 5221−5227

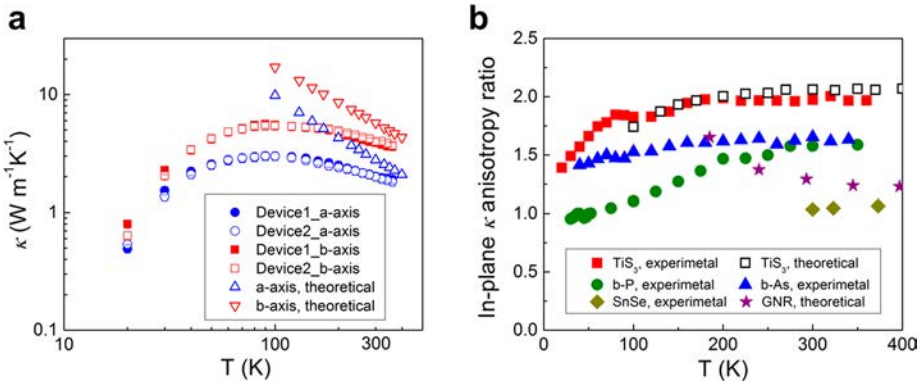

Figure 3. In-plane thermal conductivity (κ) of TiS_3 and its anisotropy. (a) Both measured and calculated temperature dependence of κ along the *a*- and *b*-axis. (b) In-plane anisotropy ratio of κ, defined as κ_b/κ_a for TiS_3 (this work), compared to the same of κ_{ZZ}/κ_{AC} for b-P (170 nm thick nanoribbon, experimental), b-As (124 nm thick nanoribbon, experimental), SnSe (bulk, experimental), and graphene nanoribbon (GNR, theoretical).

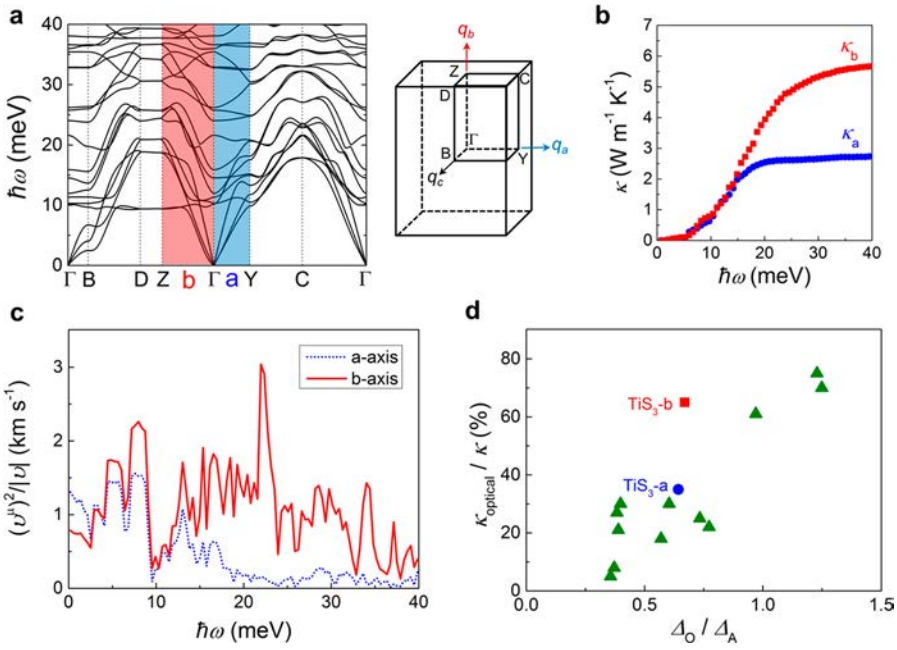

Figure 4. DFT calculation of phonon properties of TiS_3. (a) Phonon dispersion of TiS_3. The right panel shows the Brillouin zone of TiS_3. (b) Energy dependence of cumulative lattice thermal conductivity along the *a*- and *b*-axis at 300 K. (c) Average group velocity of phonon modes along the *a*- and *b*-axis, respectively, showing high anisotropy for optical phonons between 15 and 30 meV. (d) Calculated percentage of optical phonon contribution to total thermal conductivity, plotted as a function of bandwidth of the most dispersive optical phonon normalized by the bandwidth of acoustic phonons. The materials are listed in Table 1.

but they gradually become similar at lower temperatures. As shown in Figure 3b, the anisotropic ratio of κ ($=\kappa_b/\kappa_a$) remains nearly a constant of 2.0 between $T \approx 150$ and 360 K, but at $T < 150$ K the ratio is reduced toward 1.4 at $T \approx 20$ K. As a comparison, we show the in-pane anisotropy in κ of b-P,[10] b-As,[12] SnSe,[13] and graphene nanoribbon (GNR),[32] as they also possess structural anisotropy along their ZZ and AC directions in the basal plane. Their κ anisotropy (κ_{ZZ}/κ_{AC}) at 300 K is 1.6 for b-P and b-As, 1.0 for SnSe, and 1.3 for GNR. It is clear that TiS_3 hosts the highest in-plane anisotropy in κ compared to all other layered materials. Because the electrical conductivity of these TiS_3 nanoribbons is very low, about 80 and 90 S m^{-1} along the *a*- and *b*-axis at 300 K, respectively (Figure S3 in the Supporting Information), electronic contributions to κ is negligible, and the measured κ is therefore dominated by lattice thermal conductivity. Unlike the structural anisotropy arising from the ZZ versus AC bonding in b-P, b-As, SnSe, and GNR, the quasi-1D chain structure of TiS_3 is suspected to be responsible for this unusually high κ anisotropy in its basal plane.

To elucidate the physical mechanism of the anisotropic thermal conductivity in TiS_3, we calculated the phonon dispersion and thermal transport properties using density functional theory (DFT) and phonon Boltzmann transport equations via iterative solution within ShengBTE. Figure 4a shows the phonon dispersion of TiS_3 along the $\Gamma-Y$ (*a*-axis) and $\Gamma-Z$ (*b*-axis) directions in the first Brillouin zone. These results are consistent with first-principles calculations of monolayer TiS_3 reported by Zhang et al.[33]

The lattice thermal conductivity tensor, relating temperature gradient in the ν direction to heat current per unit area in the μ direction through Fourier's law, is a summation of contribu-

https://dx.doi.org/10.1021/acs.nanolett.0c01476
Nano Lett. 2020, 20, 5221−5227

tions from all phonon modes (j) over wavevectors ($\mathbf{q}$) in the first Brillouin zone,[34] written as

$$\kappa_{\mu\nu} = \frac{1}{3}\sum_{\lambda} c_{\lambda} v_{\lambda,\mu} v_{\lambda,\nu} \tau_{\lambda} \quad (1)$$

where the index $\lambda = j, \mathbf{q}$, c_λ is specific heat capacity, $v_{\lambda,\mu}$ is phonon group velocity in the μ direction, and τ_λ is phonon relaxation time. The first suspect that may cause the large anisotropy in κ would be anisotropy in acoustic phonon group velocity or anharmonicity, as demonstrated in the case of b-P.[10] However, from the dispersion relation in Figure 4a, it can be seen that the acoustic phonon group velocity does not differ significantly along the a- and b-axis directions. Indeed, as shown in Table S1 (see Supporting Information), the averaged group velocity of acoustic phonons is calculated to v_A = 4.44 km s^{-1} and 4.79 km s^{-1} along the a- and b-axis, respectively. These values differ by only ∼8%, or if comparing the velocity squared (v_A^2), differ by only ∼16%. This is far lower than the observed anisotropy in κ by a factor of 2. The anharmonicity of phonons is characterized by the Grüneisen parameter (1.91 and 1.06 simulated along the a- and b-axis at 300 K, respectively) and enables the typical three-phonon processes, which defines τ_λ at temperatures higher than the Debye temperature. However, these phonon−phonon scattering processes sample phonon modes in all phase space that is allowed by energy conservation and the Umklapp momentum restriction, effectively mixing the lattice anharmonicity along all crystal directions. Therefore, we conclude that acoustic phonons are not the primary reason for the observed 2-fold in-plane anisotropy in κ.

We now focus on contributions from the optical phonons. First, we calculated the cumulative lattice thermal conductivity along a- and b-axis at 300 K as a function of phonon energy, taking into account all three-phonon scattering processes. The results are shown in Figure 4b, where κ_b is cumulated to 5.78 W m^{-1} K^{-1} and κ_a to 2.84 W m^{-1} K^{-1} (Table S2), giving rise to the theoretical anisotropy ratio of 2 in Figure 3b. At this temperature or higher (k_BT > 26 meV), the optical phonons along both directions, having energies of 10−30 meV, are nearly fully thermally activated. More importantly, it is clear that for all phonon energies below 15 meV, i.e., mostly acoustic phonons, κ_a and κ_b show nearly identical cumulative values. They start to deviate from each other only when the phonon energy is higher than 15 meV, sampling into the optical phonon branches (Figure 4a). It can be also concluded from Figure 4b that optical phonon carried heat contributes to κ by $\kappa_{optical}/\kappa \approx 34\%$ and 66% along the a- and b-axis, respectively.

The questions arising are then (1) why optical phonons contribute to κ by such an unusually high fraction in TiS_3 and (2) why such contribution differs so much for heat flowing along the a- and b-axis.

Crystals with complex unit cell structures have a large number of optical phonon modes, and they account for a high fraction of the phonon density of states. However, they typically contribute negligibly to thermal conductivity due to their low group velocities and short lifetimes.[35] In rare cases when optical phonons become dispersive with considerable group velocities, they may contribute significantly to the total thermal conductivity. For example, it has been recently shown that optical phonons account for 22% of κ in PbTe,[36] 25% in PbSe,[36] 30% in Mg_2Si,[37] and 75% in hexagonal $Ge_2Sb_2Te_5$.[38] We found that TiS_3 is another example for such a case. Figure 4a shows that between 10 and 30 meV, there exist a large number of dispersive optical phonon modes along both the a- and b-axis direction. Especially along the b-axis direction (Γ−Z), the optical phonon modes exhibit dispersions with a slope that is nearly parallel to those of the acoustic modes, indicating an unusually high optical phonon group velocity that is comparable to that of the acoustic phonons. The values of these velocities are compared in Table S1.

Following Mukhopadhyay et al.,[38] we calculated and show in Figure 4c the energy-dependent group velocity averaged over all phonon modes along the a- and b-axis directions. This averaged velocity is calculated by

$$\bar{v}(\omega) = \frac{(v^{\mu})^2}{|v|}(\omega) = \left(\frac{\Delta q}{2\pi}\right)^3 \sum_{\lambda} \frac{(v_{\lambda}^{\mu})^2}{|v_{\lambda}^{\mu}|}\delta(\omega - \omega_{\lambda}) / \sum_{j} g_j(\omega) \quad (2)$$

where v_j^μ is the phonon group velocity of phonon mode j at wavevector $\mathbf{q}$ along the μ-axis and $g_j(\omega)$ denotes phonon density of states. Two major features are evident from Figure 4c: (I) optical phonons (between 10−30 meV) exhibit considerable group velocity, comparable to that of acoustic phonons (between 0−15 meV), and (II) this effect is much more pronounced along the b- than a-axis direction, showing a high anisotropy attributed mostly to optical phonons, rather than acoustic phonons.

Effect I is related to the high dispersiveness of the optical phonons. In a simple 1D diatomic chain model,[39] a highly dispersive optical phonon mode requires strong intracell bonding and that the two atoms do not have extreme mass ratio. Contrasted to these, the acoustic phonon group velocity depends on intercell bonding and total mass in the unit cell. These conditions are all reasonably satisfied in TiS_3. To have a high $\kappa_{optical}/\kappa$, it is also preferred that the contribution of acoustic phonons to κ ($\kappa_{acoustic}$) is low. This is indeed the case in TiS_3, where the acoustic phonons are expected to be scattered strongly via the three-phonon processes. The absence of bandgap between acoustic and optical phonons in Figure 4a facilitates the scattering of acoustic phonons by optical phonons (the so-called aao process, where "a" and "o" represent acoustic and optical phonons, respectively);[40] the well-separated (i.e., nonbunched) acoustic phonon lines provide large phase space for the scattering of acoustic phonons by each other (the so-called aaa process).[40] Taken together, these effects cause an unusually high $\kappa_{optical}/\kappa$ in TiS_3.

Effect II is attributed to the different bonding length and bonding configuration along the a- and b-axis crystallographic directions. As seen in Figure 4a, the optical phonon dispersions along the a-axis are in general flatter than along the b-axis, although several dispersive modes are also seen. This can be partially explained by the larger lattice constant, hence narrower Brillouin zone along the a-axis. Symmetry rules impose the requirement of zero slopes for these phonon modes at the zone center and boundary (e.g., at Γ, Y, and Z in Figure 4a); therefore, a narrower zone would naturally lead to flatter optical bands and consequently lower optical phonon group velocities. This effect shares the same origin as in GaAs/AlAs superlattices,[41] where in the cross-plane direction GaAs and AlAs were grown in periods equal to n times the natural unit cell of their bulk counterparts. The Brillouin zone is then folded along the cross-plane direction to a width that is $1/n$

https://dx.doi.org/10.1021/acs.nanolett.0c01476
Nano Lett. 2020, 20, 5221−5227

Table 1. Comparison of Properties of Selected Materials[a]

		mass ratio, m/M	Debye temp (K)	max acoustic bandwidth, Δ_A (meV)	max optical bandwidth, Δ_O (meV)	κ [W/(m K)], 300 K	$\kappa_{optical}/\kappa$ (%), 300 K	reference
TiS_3	*b*-axis	0.67	438	20.9	14.0	5.78	66	this work
	a-axis		300	13.9	8.9	2.84	34	
	Si	1.0	710	51.1	18.2	145	5	Broido et al.[34]
	Ge	1.0	415	29.4	10.9	60	8	Broido et al.[34]
b-P	zigzag	1.0	278	24.0	9.2	30.1	27	Qin et al.[43]
	armchair			15.6	6.0	13.6	21	Qin et al.[43]
	PbSe	0.38	170	12.7	9.3	2.2	25	Tian et al.[36]
	PbTe	0.62	140	11.5	4.0	2.0	22	Tian et al.[36]
	Bi_2Te_3, in-plane	0.61	162	7.0	4.2	1.2	30	Hellman et al.[44]
	$Ge_2Sb_2Te_5$, in-plane	0.58	100	5.8	7.1	1.7	75	Mukhopadhyay et al.[38]
	Mg_2Si	0.86	432	35.2	14.0	11.3	30	Li et al.[37]
	Mg_2Sn	0.20	273	14.6	8.3	7.2	18	Li et al.[37]
	SnSe, zigzag	0.66	210	6.9	6.7	2.0	61	Guo et al.[45]
	SnS, zigzag	0.27	270	8.0	10.0	2.3	70	Guo et al.[45]

[a] Δ_O and Δ_A are bandwidths of the most dispersive optical and acoustic phonons from calculated dispersion relation.

times of the in-plane zone width, resulting in strong suppression of optical phonon group velocity in the cross-plane direction. A similar effect exists now along the *a*- and *b*-axis directions in TiS_3, although both are in-plane. Aside from the high anisotropy in group velocity, optical phonons along these two directions do not differ much in their contribution to all three-phonon scattering processes. We calculated the relaxation lifetime of all three-phonon scattering processes, and the contributions to these processes from *a*- and *b*-axis optical phonons, and show the results in Figure S5. It can be seen that the optical phonons along these two directions do not differ significantly in their contribution to these processes. This finding further confirms the conclusion that it is the anisotropy in group velocity of the optical phonons, rather than their role in scattering acoustic phonons, that causes the large κ_b/κ_a in TiS_3.

At the atomic scale, the strong in-plane anisotropy of thermal conductivity results from the distinct atomic bonding configurations. As shown in Figure 1, only two Ti−S bonds exist along the *a*-axis direction between any two Ti atoms, while there are six Ti−S bonds along the *b*-axis direction. Moreover, the strong anisotropy of optical phonons is reflected by the strong anisotropy of the electronic polarizability of TiS_3. We calculated the Born effective charge $(e^*)_{I,\mu\nu}$ of TiS_3, which reflects the force of the atom I along μ-direction, under the electric field along ν-direction.[42] The diagonal components of the in-plane Born effective charge tensors are shown in Table S3, which shows that $(e^*)_{bb}$ is much larger than $(e^*)_{aa}$ for all Ti and S atoms. For example, for the Ti1(Ti2) and S3(S4) atoms, the ratio of $(e^*)_{bb}/(e^*)_{aa}$ is 2−3, while for the atoms S1(S2) and S5(S6), $(e^*)_{aa}$ are even smaller compared to $(e^*)_{bb}$. As is well-known, the optical modes correspond to the opposite displacement of positive and negative charged atoms, generating internal electric fields in the crystal. The magnitude of the restoration force of each atom depends on its Born effective charge. Consequently, the interactions along the *b*-axis will be stronger than those along the *a*-axis direction. The optical phonons are usually closely related to the dielectric permittivity. Therefore, it is expected that the dielectric constant would also be highly anisotropic in TiS_3. Indeed, our DFT results show that the static dielectric constant in TiS_3 are 12.51 and 33.15 along its *a*- and *b*-axis directions, respectively.

We also calculated the temperature dependence of κ along the two in-plane directions using DFT, including all possible phonon−phonon interactions but not phonon-impurity and phonon-boundary scatterings. As shown in Figure 3, although the values of the calculated κ are slightly higher than the measured values, their ratio, κ_b/κ_a, agrees well with the measurements.

We now compare all reported materials that show a high percentage of $\kappa_{optical}/\kappa$ in an attempt to find properties in common. As seen from eq 1, it is not surprising that these materials typically have at least one optical phonon branch that is highly dispersive and thus has high group velocity to carry heat flow. The high dispersiveness would lead to large bandwidth for that phonon mode over the Brillouin zone. We define the normalized bandwidth (Δ_O/Δ_A) as the bandwidth of the most dispersive optical phonon (Δ_O) divided by that (Δ_A) of the most dispersive acoustic phonon. In a simple diatomic chain model, a high Δ_O/Δ_A prefers similar masses of the two atoms, as well as stronger spring constant for vibration modes involving the lighter atoms than for the heavier atoms. From published calculated phonon dispersions of a selected set of materials including TiS_3 (Table 1), we plot in Figure 4d $\kappa_{optical}/\kappa$ as a function of Δ_O/Δ_A. A positive correlation can be seen between these two quantities. The data scattering reflects factors missing in the plot: the lifetime ratio between optical and acoustic phonons differ in different materials, and only the single, most dispersive optical and acoustic phonons are considered. Nevertheless, the approximate correlation shows that optical phonons may contribute a large portion to lattice thermal conductivity in materials with one or more highly dispersive optical phonons. In TiS_3, along *b*-axis more highly dispersive optical phonon branches with high group velocity contribute to carrying heat flow, leading to an unusually high portion of $\kappa_{optical}/\kappa$, as shown in Figure 4d.

In conclusion, we found an extreme anisotropy, by a factor of 2 and higher than that of any existing layered materials, in the in-plane thermal conductivity in TiS_3. This occurs between the quasi-1D chain direction and the interchain direction in the basal plane of this layered material. First-principles calculations reveal that, unlike most materials where heat is mostly

https://dx.doi.org/10.1021/acs.nanolett.0c01476
Nano Lett. 2020, 20, 5221−5227

transported by acoustic phonons, in TiS_3 the optical phonons carry an unusually high portion of heat, up to 66% along the chain direction, owing to highly dispersive optical phonons. Perpendicular to the chain direction, however, the optical phonons are less dispersive and contribute to a much lower 34% of thermal conductivity. With such highly anisotropic thermal transport in the basal plane, layered TiS_3 may serve as a platform for designing novel devices to route heat flow at the nanoscale, such as thermal switch, regulator, or diodes.[46]

■ ASSOCIATED CONTENT

Supporting Information

The Supporting Information is available free of charge at https://pubs.acs.org/doi/10.1021/acs.nanolett.0c01476.

Experimental details, phonon dispersion and thermal properties, Born effective charge tensor; figures of optical images, electrical characterization, temperature dependence of σ and S, phonon dispersion, relaxation time vs optical phonon energy, Partial phonon density of states, Percentage of contribution to κ, electronic band structure, crystal structure, height profile, thermal conductivity, measured thermal conductance, and cumulative thermal conductivity vs phonon mean free path; tables of velocities, thermal conductivities, and Born effective charge tensors (PDF)

■ AUTHOR INFORMATION

Corresponding Authors

Junqiao Wu − *Materials Sciences Division, Lawrence Berkeley National Laboratory, Berkeley, California 94720, United States; Department of Materials Science and Engineering, University of California, Berkeley, California 94720, United States;* orcid.org/0000-0002-1498-0148; Email: wuj@berkeley.edu

Jiawang Hong − *School of Aerospace Engineering, Beijing Institute of Technology, Beijing 100081, China;* orcid.org/0000-0002-9915-8072; Email: hongjw@bit.edu.cn

Lidong Chen − *State Key Laboratory of High Performance Ceramics and Superfine Microstructure, Shanghai Institute of Ceramics, Chinese Academy of Sciences, Shanghai 200050, China*; Email: cld@mail.sic.ac.cn

Authors

Huili Liu − *Materials Sciences Division, Lawrence Berkeley National Laboratory, Berkeley, California 94720, United States; Department of Materials Science and Engineering, University of California, Berkeley, California 94720, United States;* orcid.org/0000-0001-8959-0315

Xiaoxia Yu − *School of Aerospace Engineering, Beijing Institute of Technology, Beijing 100081, China*

Kedi Wu − *School for Engineering of Matter, Transport, and Energy, Arizona State University, Tempe, Arizona 85287, United States;* orcid.org/0000-0003-4160-2457

Yang Gao − *Materials Sciences Division, Lawrence Berkeley National Laboratory, Berkeley, California 94720, United States; Department of Materials Science and Engineering, University of California, Berkeley, California 94720, United States*

Sefaattin Tongay − *School for Engineering of Matter, Transport, and Energy, Arizona State University, Tempe, Arizona 85287, United States;* orcid.org/0000-0001-8294-984X

Ali Javey − *Materials Sciences Division, Lawrence Berkeley National Laboratory, Berkeley, California 94720, United States; Department of Electrical Engineering and Computer Science, University of California, Berkeley, California 94720, United States;* orcid.org/0000-0001-7214-7931

Complete contact information is available at: https://pubs.acs.org/10.1021/acs.nanolett.0c01476

Author Contributions

H.L. and J.W. conceived the project. H.L. designed the experiments, fabricated devices, and performed thermal and electrical measurements. X.Y. and J.H. performed the theoretical calculation. K.W. and S.T. provided the single crystal flake and SEM characterization of sample. H.L., X.Y., J.H. and J.W. discussed the data. H.L. and J.W. wrote the manuscript. All authors contributed to discussing the data and editing the manuscript.

Author Contributions

[#]These authors contributed equally to this work.

Notes

The authors declare no competing financial interest.

■ ACKNOWLEDGMENTS

This work was supported by the Electronic Materials Program at the Lawrence Berkeley National Laboratory, which is supported by the Office of Science, Office of Basic Energy Sciences, of the U.S. Department of Energy under Contract No. DE-AC02-05CH11231. J.H. acknowledges the support from the National Science Foundation of China (Grant No. 11572040), Beijing Natural Science Foundation (Grant No. Z190011), and the Technological Innovation Project of Beijing Institute of Technology. Theoretical calculations were performed using resources of National Supercomputer Center in Guangzhou. We thank Dr. Bin Chen for SEM characterization of sample. We thank Prof. Feng Wang and Dr. Saikat Mukhopadhyay for insightful discussions.

■ REFERENCES

(1) Novoselov, K. S.; Geim, A. K.; Morozov, S. V.; Jiang, D.; Zhang, Y.; Dubonos, S. V.; Grigorieva, I. V.; Firsov, A. A. Electric field effect in atomically thin carbon films. *Science* **2004**, *306*, 666−669.

(2) Castro Neto, A. H.; Guinea, F.; Peres, N. M. R.; Novoselov, K. S.; Geim, A. K. The electronic properties of graphene. *Rev. Mod. Phys.* **2009**, *81*, 109−162.

(3) Mak, K. F.; Lee, C.; Hone, J.; Shan, J.; Heinz, T. F. Atomically thin MoS_2: a new direct-gap semiconductor. *Phys. Rev. Lett.* **2010**, *105*, 136805.

(4) Deng, D.; Novoselov, K. S.; Fu, Q.; Zheng, N.; Tian, Z.; Bao, X. Catalysis with two-dimensional materials and their heterostructures. *Nat. Nanotechnol.* **2016**, *11*, 218−230.

(5) Bonaccorso, F.; Sun, Z.; Hasan, T.; Ferrari, A. C. Graphene photonics and optoelectronics. *Nat. Photonics* **2010**, *4*, 611−622.

(6) Wang, Q. H.; Kalantar-Zadeh, K.; Kis, A.; Coleman, J. N.; Strano, M. S. Electronics and optoelectronics of two-dimensional transition metal dichalcogenides. *Nat. Nanotechnol.* **2012**, *7*, 699−712.

(7) Roy, K.; Padmanabhan, M.; Goswami, S.; Sai, T. P.; Ramalingam, G.; Raghavan, S.; Ghosh, A. Graphene-MoS_2 hybrid structures for multifunctional photoresponsive memory devices. *Nat. Nanotechnol.* **2013**, *8*, 826−830.

(8) Britnell, L.; Ribeiro, R. M.; Eckmann, A.; Jalil, R.; Belle, B. D.; Mishchenko, A.; Kim, Y. J.; Gorbachev, R. V.; Georgiou, T.; Morozov, S. V.; Grigorenko, A. N.; Geim, A. K.; Casiraghi, C.; Castro Neto, A. H.; Novoselov, K. S. Strong light-matter interactions in heterostructures of atomically thin films. *Science* **2013**, *340*, 1311−1314.

(9) Coleman, J. N.; Lotya, M.; O'Neill, A.; Bergin, S. D.; King, P. J.; Khan, U.; Young, K.; Gaucher, A.; De, S.; Smith, R. J.; Shvets, I. V.; Arora, S. K.; Stanton, G.; Kim, H.-Y.; Lee, K.; Kim, G. T.; Duesberg, G. S.; Hallam, T.; Boland, J. J.; Wang, J. J.; Donegan, J. F.; Grunlan, J. C.; Moriarty, G.; Shmeliov, A.; Nicholls, R. J.; Perkins, J. M.; Grieveson, E. M.; Theuwissen, K.; McComb, D. W.; Nellist, P. D.; Nicolosi, V. Two-dimensional nanosheets produced by liquid exfoliation of layered materials. *Science* **2011**, *331*, 568−571.
(10) Lee, S.; Yang, F.; Suh, J.; Yang, S.; Lee, Y.; Li, G.; Choe, H.; Suslu, A.; Chen, Y.; Ko, C.; Park, J.; Liu, K.; Li, J.; Hippalgaonkar, K.; Urban, J. J.; Tongay, S.; Wu, J. Anisotropic in-plane thermal conductivity of black phosphorus nanoribbons at temperatures higher than 100 K. *Nat. Commun.* **2015**, *6*, 8573.
(11) Liu, H.; Choe, H. S.; Chen, Y.; Suh, J.; Ko, C.; Tongay, S.; Wu, J. Variable range hopping electric and thermoelectric transport in anisotropic black phosphorus. *Appl. Phys. Lett.* **2017**, *111*, 102101.
(12) Chen, Y.; Chen, C.; Kealhofer, R.; Liu, H.; Yuan, Z.; Jiang, L.; Suh, J.; Park, J.; Ko, C.; Choe, H. S.; Avila, J.; Zhong, M.; Wei, Z.; Li, J.; Li, S.; Gao, H.; Liu, Y.; Analytis, J.; Xia, Q.; Asensio, M. C.; Wu, J. Black arsenic: a layered semiconductor with extreme in-plane anisotropy. *Adv. Mater.* **2018**, *30*, 1800754.
(13) Zhao, L.-D.; Lo, S.-H.; Zhang, Y.; Sun, H.; Tan, G.; Uher, C.; Wolverton, C.; Dravid, V. P.; Kanatzidis, M. G. Ultralow thermal conductivity and high thermoelectric figure of merit in SnSe crystals. *Nature* **2014**, *508*, 373−377.
(14) Son, Y.-W.; Cohen, M. L.; Louie, S. G. Energy gaps in graphene nanoribbons. *Phys. Rev. Lett.* **2006**, *97*, 216803.
(15) Manzeli, S.; Ovchinnikov, D.; Pasquier, D.; Yazyev, O. V.; Kis, A. 2D transition metal dichalcogenides. *Nature Reviews Materials* **2017**, *2*, 17033.
(16) Jin, Y.; Li, X.; Yang, J. Single layer of MX_3 (M = Ti, Zr; X = S, Se, Te): a new platform for nano-electronics and optics. *Phys. Chem. Chem. Phys.* **2015**, *17*, 18665−18669.
(17) Island, J. O.; Biele, R.; Barawi, M.; Clamagirand, J. M.; Ares, J. R.; Sánchez, C.; van der Zant, H. S. J.; Ferrer, I. J.; D'Agosta, R.; Castellanos-Gomez, A. Titanium trisulfide (TiS_3): a 2D semiconductor with quasi-1D optical and electronic properties. *Sci. Rep.* **2016**, *6*, 22214.
(18) Gorlova, I. G.; Pokrovskii, V. Y.; Zybtsev, S. G.; Titov, A. N.; Timofeev, V. N. Features of the conductivity of the quasi-one-dimensional compound TiS_3. *J. Exp. Theor. Phys.* **2010**, *111*, 298−303.
(19) Furuseth, S.; Brattaas, L.; Kjekshus, A. On the crystal structures of TiS_3, ZrS_3, $ZrSe_3$, $ZrTe_3$, HfS_3, and $HfSe_3$. *Acta Chem. Scand.* **1975**, *29*, 623−631.
(20) Ferrer, I. J.; Ares, J. R.; Clamagirand, J. M.; Barawi, M.; Sánchez, C. Optical properties of titanium trisulphide (TiS_3) thin films. *Thin Solid Films* **2013**, *535*, 398−401.
(21) Kang, J.; Wang, L.-W. Robust band gap of TiS_3 nanofilms. *Phys. Chem. Chem. Phys.* **2016**, *18*, 14805−14809.
(22) Lipatov, A.; Wilson, P. M.; Shekhirev, M.; Teeter, J. D.; Netusil, R.; Sinitskii, A. Few-layered titanium trisulfide (TiS_3) field-effect transistors. *Nanoscale* **2015**, *7*, 12291−12296.
(23) Island, J. O.; Barawi, M.; Biele, R.; Almazán, A.; Clamagirand, J. M.; Ares, J. R.; Sánchez, C.; van der Zant, H. S. J.; Álvarez, J. V.; D'Agosta, R.; Ferrer, I. J.; Castellanos-Gomez, A. TiS_3 transistors with tailored morphology and electrical properties. *Adv. Mater.* **2015**, *27*, 2595−2601.
(24) Wu, K.; Torun, E.; Sahin, H.; Chen, B.; Fan, X.; Pant, A.; Wright, D. P.; Aoki, T.; Peeters, F. M.; Soignard, E.; Tongay, S. Unusual lattice vibration characteristics in whiskers of the pseudo-one-dimensional titanium trisulfide TiS_3. *Nat. Commun.* **2016**, *7*, 12952.
(25) Furuseth, S.; Fjellvåg, H.; Johansson, L.-G.; Gultyai, V. P.; Persson, I.; Elding, L. I. Re-examination of the crystal structure of $ZrTe_3$. *Acta Chem. Scand.* **1991**, *45*, 694−697.
(26) Fleet, M. E.; Harmer, S. L.; Liu, X.; Nesbitt, H. W. Polarized X-ray absorption spectroscopy and XPS of TiS_3: S K- and Ti L-edge XANES and S and Ti 2p XPS. *Surf. Sci.* **2005**, *584*, 133−145.
(27) Cordero, B.; Gómez, V.; Platero-Prats, A. E.; Revés, M.; Echeverría, J.; Cremades, E.; Barragán, F.; Alvarez, S. Covalent radii revisited. *Dalton Transactions* **2008**, 2832−2838.
(28) Silva-Guillén, J. A.; Canadell, E.; Ordejón, P.; Guinea, F.; Roldán, R. Anisotropic features in the electronic structure of the two-dimensional transition metal trichalcogenide TiS_3: electron doping and plasmons. *2D Mater.* **2017**, *4*, 025085.
(29) Shi, L.; Li, D.; Yu, C.; Jang, W.; Kim, D.; Yao, Z.; Kim, P.; Majumdar, A. Measuring thermal and thermoelectric properties of one-dimensional nanostructures using a microfabricated device. *J. Heat Transfer* **2003**, *125*, 881−888.
(30) Li, D.; Wu, Y.; Kim, P.; Shi, L.; Yang, P.; Majumdar, A. Thermal conductivity of individual silicon nanowires. *Appl. Phys. Lett.* **2003**, *83*, 2934−2936.
(31) Lee, S.; Hippalgaonkar, K.; Yang, F.; Hong, J.; Ko, C.; Suh, J.; Liu, K.; Wang, K.; Urban, J. J.; Zhang, X.; Dames, C.; Hartnoll, S. A.; Delaire, O.; Wu, J. Anomalously low electronic thermal conductivity in metallic vanadium dioxide. *Science* **2017**, *355*, 371−374.
(32) Hu, J.; Ruan, X.; Chen, Y. P. Thermal conductivity and thermal rectification in graphene nanoribbons: a molecular dynamics study. *Nano Lett.* **2009**, *9*, 2730−2735.
(33) Zhang, J.; Liu, X.; Wen, Y.; Shi, L.; Chen, R.; Liu, H.; Shan, B. Titanium trisulfide monolayer as a potential thermoelectric material: a first-principles-based boltzmann transport study. *ACS Appl. Mater. Interfaces* **2017**, *9*, 2509−2515.
(34) Broido, D. A.; Malorny, M.; Birner, G.; Mingo, N.; Stewart, D. A. Intrinsic lattice thermal conductivity of semiconductors from first principles. *Appl. Phys. Lett.* **2007**, *91*, 231922.
(35) Ashcroft, N. W.; Mermin, N. D. *Solid State Physics*; Holt, Rinehart and Winston: New York, 1976.
(36) Tian, Z.; Garg, J.; Esfarjani, K.; Shiga, T.; Shiomi, J.; Chen, G. Phonon conduction in PbSe, PbTe, and $PbTe_{1-x}Se_x$ from first-principles calculations. *Phys. Rev. B: Condens. Matter Mater. Phys.* **2012**, *85*, 184303.
(37) Li, W.; Lindsay, L.; Broido, D. A.; Stewart, D. A.; Mingo, N. Thermal conductivity of bulk and nanowire $Mg_2Si_xSn_{1-x}$ alloys from first principles. *Phys. Rev. B: Condens. Matter Mater. Phys.* **2012**, *86*, 174307.
(38) Mukhopadhyay, S.; Lindsay, L.; Singh, D. J. Optic phonons and anisotropic thermal conductivity in hexagonal $Ge_2Sb_2Te_5$. *Sci. Rep.* **2016**, *6*, 37076.
(39) Kittel, C. *Introduction to Solid State Physics*, 7th ed.; Wiley: New York, 1996.
(40) Lindsay, L.; Broido, D. A.; Reinecke, T. L. First-principles determination of ultrahigh thermal conductivity of boron arsenide: a competitor for diamond? *Phys. Rev. Lett.* **2013**, *111*, 025901.
(41) Bies, W. E.; Radtke, R. J.; Ehrenreich, H. Phonon dispersion effects and the thermal conductivity reduction in GaAs/AlAs superlattices. *J. Appl. Phys.* **2000**, *88*, 1498−1503.
(42) Gonze, X.; Lee, C. Dynamical matrices, Born effective charges, dielectric permittivity tensors, and interatomic force constants from density-functional perturbation theory. *Phys. Rev. B: Condens. Matter Mater. Phys.* **1997**, *55*, 10355−10368.
(43) Qin, G.; Yan, Q.-B.; Qin, Z.; Yue, S.-Y.; Hu, M.; Su, G. Anisotropic intrinsic lattice thermal conductivity of phosphorene from first principles. *Phys. Chem. Chem. Phys.* **2015**, *17*, 4854−4858.
(44) Hellman, O.; Broido, D. A. Phonon thermal transport in Bi_2Te_3 from first principles. *Phys. Rev. B: Condens. Matter Mater. Phys.* **2014**, *90*, 134309.
(45) Guo, R.; Wang, X.; Kuang, Y.; Huang, B. First-principles study of anisotropic thermoelectric transport properties of IV-VI semiconductor compounds SnSe and SnS. *Phys. Rev. B: Condens. Matter Mater. Phys.* **2015**, *92*, 115202.
(46) Wehmeyer, G.; Yabuki, T.; Monachon, C.; Wu, J.; Dames, C. Thermal diodes, regulators, and switches: physical mechanisms and potential applications. *Appl. Phys. Rev.* **2017**, *4*, 041304.

https://dx.doi.org/10.1021/acs.nanolett.0c01476
Nano Lett. 2020, 20, 5221−5227

Supporting Information for

Extreme in-plane thermal conductivity anisotropy in titanium trisulfide caused by heat-carrying optical phonons

Huili Liu[†,‡,§], *Xiaoxia Yu*[£,§], *Kedi Wu*[¶], *Yang Gao*[†,‡], *Sefaattin Tongay*[¶], *Ali Javey* [†, Î], *Lidong Chen*[€,*], *Jiawang Hong*[£,*] *and Junqiao Wu*[†,‡,*]

[†]Materials Sciences Division, Lawrence Berkeley National Laboratory, Berkeley, California 94720, USA

[‡]Department of Materials Science and Engineering, University of California, Berkeley, California 94720, USA

[£]School of Aerospace Engineering, Beijing Institute of Technology, Beijing 100081, China

[¶]School for Engineering of Matter, Transport, and Energy, Arizona State University, Tempe, Arizona 85287, USA

[Î]Department of Electrical Engineering and Computer Science, University of California, Berkeley, California 94720, USA

[€]State Key Laboratory of High Performance Ceramics and Superfine Microstructure, Shanghai Institute of Ceramics, Chinese Academy of Sciences, Shanghai, 200050, China

[§]Those authors contributed equally to this work

*Author to whom correspondence should be addressed. Electronical mail: wuj@berkeley.edu, hongjw@bit.edu.cn, cld@mail.sic.ac.cn

Experimental details. *TiS_3 nanoribbon device fabrication*. TiS_3 single crystals, shown in Figure S1, grow naturally into micro-ribbons or whiskers parallel to its b-axis direction.[1] As reported previously,[2, 3] TiS_3 flakes were mechanically exfoliated onto a SiO_2/Si substrate using PDMS (Polydimethylsiloxane), and then tailored into nanoribbons (0.5 - 2 μm in width and 25 - 40 μm in length) using electron-beam lithography (EBL) followed by reactive ion etching (RIE). Specifically, the flakes were coated by PMMA (Poly(methyl methacrylate), C4-950, 4000 rpm) and baked at 180 °C for 5 mins. The PMMA was patterned with EBL followed by a developing process using MIBK : IPA = 1 : 3 for 1 min. The exposed TiS_3 was etched via RIE using a mixed gas (90% SF_6 and 10% O_2, 60 sccm) for several seconds. After the PMMA removal with acetone and rinsing by isopropyl alcohol, TiS_3 nanoribbons were obtained. The thickness of the nanoribbon was confirmed by Atomic Force Microscope (AFM), as shown in Figure 2 and Figure S10. Selected individual nanoribbon was manually dry-transferred onto an empty, suspended-pad micro-device using a sharp Tungsten needle (600 nm tip diameter, Cascade Microtech). The electrical quality of the electrodes was verified by a linear I-V relationship (ohmic contact). To further improve the electrical and thermal contact, a small amount of Pt metal was deposited by focused ion beam (FIB, dual-beam FEI Quanta) to bond the end of the nanoribbon to the underneath metal electrodes (Figure 2d and 2e). Indeed, the electrical contact resistance is reduced after the FIB Pt deposition, as shown in Figure S2. The devices were annealed at 373 K for one hour in vacuum to further improve electrical and thermal contacts at the electrodes.

Thermal and electrical measurements. The thermal resistance, electrical conductance, and Seebeck coefficient of nanoribbons were measured using the suspended-pad micro-devices technique following previous reports.[4, 5] Two SiN_x pads with Pt electrodes were suspended by

long and flexible SiN_x arms (~400 μm). Pt serpentine electrodes on the pads were for micro-heater and thermometers, and additional four Pt electrodes were for electrical resistance and thermopower measurements. A DC current (I = 0-15 μA) was applied to the micro-heater for the temperature raising (hot pad) of ΔT_h, and the other pad (cold pad) sensed a temperature of ΔT_c through the nanoribbon. An external heater (Lakeshore 335 Temperature Controller) and cryogenic compressor cooler (HC-4A, Sumitomo CRYOGENICS) controlled the global temperature in the chamber, which was under high vacuum (< 10^{-6} Torr) during the measurements. An AC current with a small amplitude of ~ 500 nA and frequency of 1.1 kHz (199 Hz) was applied to probe ΔT_h (ΔT_c) on the hot (cold) pad using Lock-in amplifiers. The thermal conductance of the nanoribbon (G) is given by $G = (Q \times \Delta T_c)/(\Delta T_h^2 - \Delta T_c^2)$, where Q is the heating power, $Q = I^2 \times (R_h + R_{arm})$, and R_h and R_{arm} are the resistance of heating Pt electrodes and arms, respectively. Electrical resistance was measured by the four-probe method using a Keithley nanovoltmeter (2182A) and precision current source (6220). The dimensions of nanoribbons were determined by Scanning Electron Microscope (SEM) and AFM. Data errors were estimated as ~8% for thermal conductivity, and ~5% for electrical conductivity and Seebeck coefficient. The length dependence of thermal conductance was performed for several nanoribbons from the same flake. Figure 2f shows cross-sectional area divided by thermal conductance (A/G) as a function of the nanoribbon length (L), where a linear relationship is seen and extrapolated to nearly zero A/G at L = 0, proving negligible contact thermal resistance for these nanoribbons devices. Figure 3a and Figure S11 show the in-plane thermal conductivity of TiS_3 of two devices along a- and b-axis, respectively. Figure S12 shows the measured thermal conductance at 300 K for Device2_b-axis, where the raising temperature of hot pad and cold pad is ΔT_h = 0 – 4.6 K and ΔT_c = 0 - 1.4 K, respectively. The measured heat flow through the

nanoribbon increases linearly with the temperature difference between hot pad and cold pad, ΔT_h - ΔT_c = 0 – 3.2 K, as shown in Figure S12b, therefore the thermal conductance is 46.4 nW K^{-1} at 300 K for Device2_b-axis.

Theoretical calculation. First-principles electronic structure calculations of TiS_3 were performed using density functional theory (DFT) within the generalized gradient approximation (GGA). The Perdue-Burke-Erznerhof (PBE) form was used for the exchange-correlation functional.[6] The projector-augmented plane wave basis method as implemented in VASP (Vienna *ab initio* simulation package)[7] was used for all structural relaxations and supercell calculations for interatomic force constants. A 8×10×4 Monkhorst-Pack *k*-point grid and a plane wave energy cutoff of 500 eV was used for all structural relaxations. We used the DFT-D2 method as implemented in VASP for describing the weak vdW interaction between TiS_3 layers. The convergence threshold for energy and forces was set to 10^{-7} eV and 10^{-4} eV/Å, respectively. In the supercell calculations for obtaining harmonic (second order) interatomic force constants (IFCs) and anharmonic (third order) IFCs, Phonopy[8] and ShengBTE code[9] were used by taking into consideration non-analytical term correction and the force constant calculations were done with a same 2×3×2 supercell and a 4×3×2 *q*-point mesh, until convergence threshold above all was satisfied. The simulated lattice constants: a = 4.97 Å, b = 3.93 Å, c = 8.80 Å, are in consistency with literature.[10, 11]

Note 1. Phonon dispersion and thermal properties

The simulated phonon dispersion is shown in Figure S4. No imaginary part exists, indicating thermodynamic stability for the cell. In TiS_3, there are 3 acoustic modes and 21 optical modes, corresponding to 8 atoms per primitive unit cell. The phonon dispersions with DFT are

consistent with experimental Raman data[1] shown in Figure S4. Indeed, in the energy range of ~10 - 30 meV, phonon modes (optical phonons) are more dispersive along the Γ- Z direction (b-axis) than along the Γ- Y direction (a-axis). These lattice vibrations are mostly associated with sulfur atoms, as shown in the phonon DOS plot in Figure S4, leading to anisotropy in optical phonon DOS as shown in Figure S6. Above ~30 meV, it is seen that all optical phonons are less dispersive, have small group velocity, and do not carry heat. The anisotropy of group velocities is tabulated in Table S1. The average group velocity for optical modes is 1.02 km s^{-1} along the b-axis, much higher than 0.49 km s^{-1}along a-axis. Thermal conductivity of optical modes at 300 K along the b-axis is predicated to 3.74 W m^{-1} K^{-1}, in stark contrast to 0.97 W m^{-1} K^{-1} along a-axis. In conclusion, the low-lying optical modes between ~15 - 30 meV play the essential role in heat conduction, and dominate the extreme in-plane anisotropy in thermal conductivity of TiS_3. Figure S7 shows the percentage of contribution to κ from different phonon modes, where it is shown that significant contributions to thermal conductivity are mainly from the optical modes of No. 4 - 13 in the range of ~15 - 30 meV. The Mode 8 shows a prominent optical vibration with large dispersiveness, and the atomic vibrations of this mode is shown in Figure S9b. Figure S13 shows the cumulative thermal conductivity versus phonon mean free path (MFP) along a- and b-axis at 300 K, 100 K, and 50K, respectively. At 300 K, the average phonon mean free path is in the range of 2 - 10 nm, much smaller than the nanoribbon thickness (~ 100 nm). However, at 50 K, the average MFP increases to the range of 50 - 200 nm, comparable to the thickness of nanoribbons. Therefore, at low temperatures boundary scattering becomes dominant in the phonon transport, leading to large difference between the calculated and measured thermal conductivity in Figure 3a.

Note 2. Born effective charge tensor

The Born effective charge tensor of the atom *I*, is defined as the induced polarization (*P*) of the solid along the μ direction by a displacement (δ) in the ν direction of the sublattice of the atom *I*, which is also described by the linear relationship between the force (*F*) on the atom and the macroscopic electric field (*E*),[12]

$$(e^*)_{I,\mu\nu} = \Omega_0 \frac{\partial P_\mu}{\partial \delta_{I,\nu}} = \frac{\partial F_{I,\nu}}{\partial E_\mu} \qquad \text{S(1)}$$

Born effective charge tensor can be calculated using density functional perturbation theory (DFPT) or within the finite-difference method (FDM), which can be used to estimate the polarization according to eq S1. The in-plane Born effective charge tensor for Ti and S in TiS_3 is tabulated in Table S3.

REFERENCES

(1) Wu, K.; Torun, E.; Sahin, H.; Chen, B.; Fan, X.; Pant, A.; Wright, D. P.; Aoki, T.; Peeters, F. M.; Soignard, E.; Tongay, S. Unusual lattice vibration characteristics in whiskers of the pseudo-one-dimensional titanium trisulfide TiS_3. *Nat. Commun.* **2016**, *7*, 12952.

(2) Lee, S.; Yang, F.; Suh, J.; Yang, S.; Lee, Y.; Li, G.; Sung Choe, H.; Suslu, A.; Chen, Y.; Ko, C.; Park, J.; Liu, K.; Li, J.; Hippalgaonkar, K.; Urban, J. J.; Tongay, S.; Wu, J. Anisotropic in-plane thermal conductivity of black phosphorus nanoribbons at temperatures higher than 100 K. *Nat. Commun.* **2015**, *6*, 8573.

(3) Liu, H.; Choe, H. S.; Chen, Y.; Suh, J.; Ko, C.; Tongay, S.; Wu, J. Variable range hopping electric and thermoelectric transport in anisotropic black phosphorus. *Appl. Phys. Lett.* **2017**, *111*, (10), 102101.

(4) Lee, S.; Hippalgaonkar, K.; Yang, F.; Hong, J.; Ko, C.; Suh, J.; Liu, K.; Wang, K.; Urban,

J. J.; Zhang, X.; Dames, C.; Hartnoll, S. A.; Delaire, O.; Wu, J. Anomalously low electronic thermal conductivity in metallic vanadium dioxide. *Science* **2017**, *355*, 371-374.

(5) Shi, L.; Li, D.; Yu, C.; Jang, W.; Kim, D.; Yao, Z.; Kim, P.; Majumdar, A. Measuring thermal and thermoelectric properties of one-dimensional nanostructures using a microfabricated device. *J. Heat Transfer* **2003**, *125*, 881-888.

(6) Perdew, J. P.; Burke, K.; Ernzerhof, M. Generalized gradient approximation made simple. *Phys. Rev. Lett.* **1996**, *77*, 3865-3868.

(7) Kresse, G.; Furthmüller, J. Efficient iterative schemes for ab initio total-energy calculations using a plane-wave basis set. *Phys. Rev. B* **1996**, *54*, 11169-11186.

(8) Togo, A.; Oba, F.; Tanaka, I. First-principles calculations of the ferroelastic transition between rutile-type and $CaCl_2$-type SiO_2 at high pressures. *Phys. Rev. B* **2008**, *78*, 134106.

(9) Li, W.; Carrete, J.; A. Katcho, N.; Mingo, N. ShengBTE: A solver of the Boltzmann transport equation for phonons. *Comput. Phys. Commun.* **2014**, *185*, 1747-1758.

(10) Zhang, J.; Liu, X.; Wen, Y.; Shi, L.; Chen, R.; Liu, H.; Shan, B. Titanium trisulfide monolayer as a potential thermoelectric material: a first-principles-based boltzmann transport study. *ACS Appl. Mater. Interfaces* **2017**, *9*, 2509-2515.

(11) Wu, J.; Wang, D.; Liu, H.; Lau, W.-M.; Liu, L.-M. An ab initio study of TiS_3: a promising electrode material for rechargeable Li and Na ion batteries. *RSC Advances* **2015**, *5*, 21455-21463.

(12) Gonze, X.; Lee, C. Dynamical matrices, Born effective charges, dielectric permittivity tensors, and interatomic force constants from density-functional perturbation theory. *Phys. Rev. B* **1997**, *55*, 10355-10368.

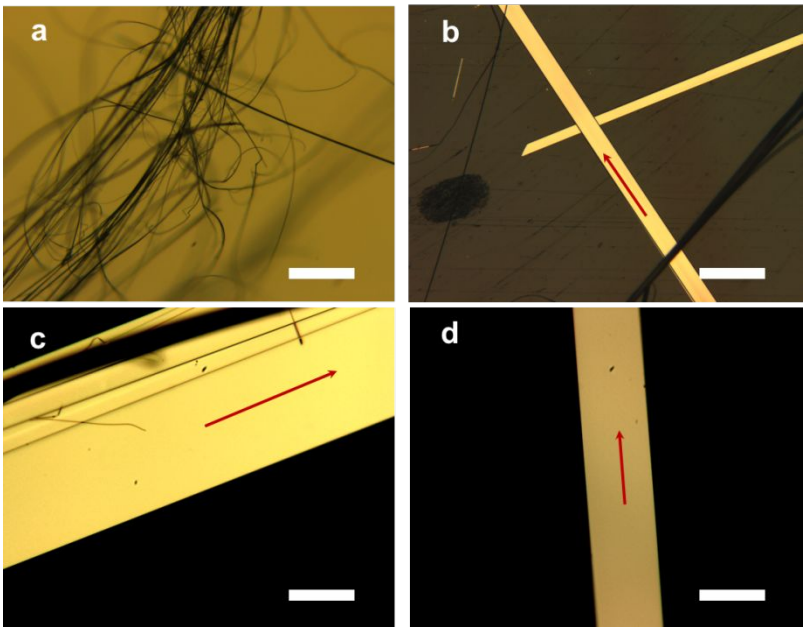

Figure S1. Optic images of TiS_3 single crystal whiskers, showing the natural geometric anisotropy. The red arrows indicate the natural chain direction (along the b-axis). Scale bars, 1 mm (a); 200 μm (b); 50 μm (c), (d).

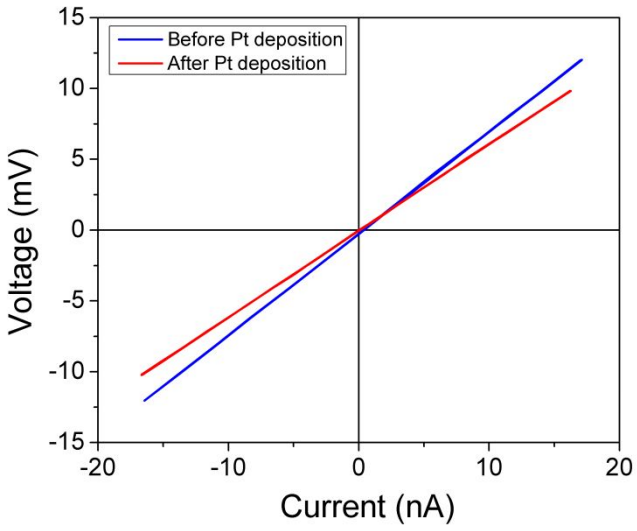

Figure S2. Electrical characterization before and after deposition of a small amount of Pt, bonding the nanoribbon onto the underlying electrodes. The electrical contact resistance is

reduced after the Pt deposition by FIB.

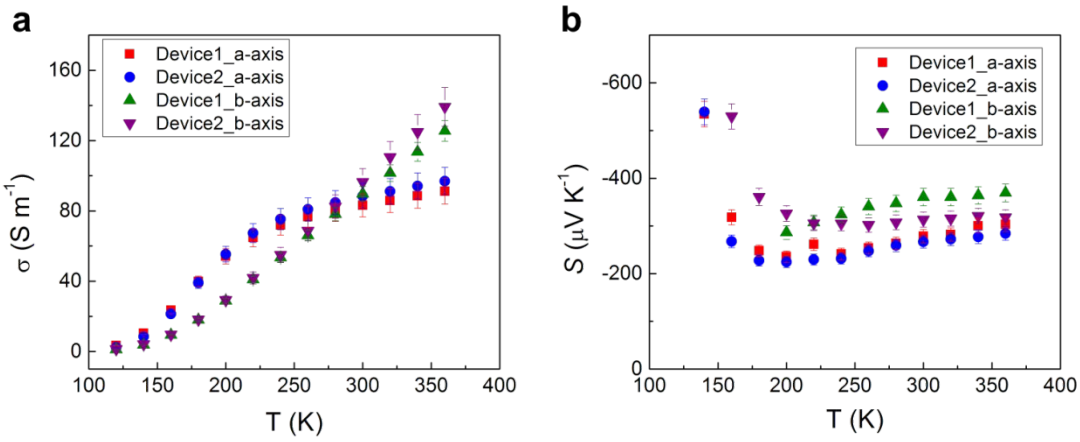

Figure S3. Temperature dependence of electrical conductivity (σ) and Seebeck coefficient (S) of TiS_3 along its a- and b-axis, respectively. Electrical conductivity shows significant anisotropy between the a- and b-axis. Seebeck coefficient shows a slight anisotropy, behaving as a typical non-degenerate semiconductor.

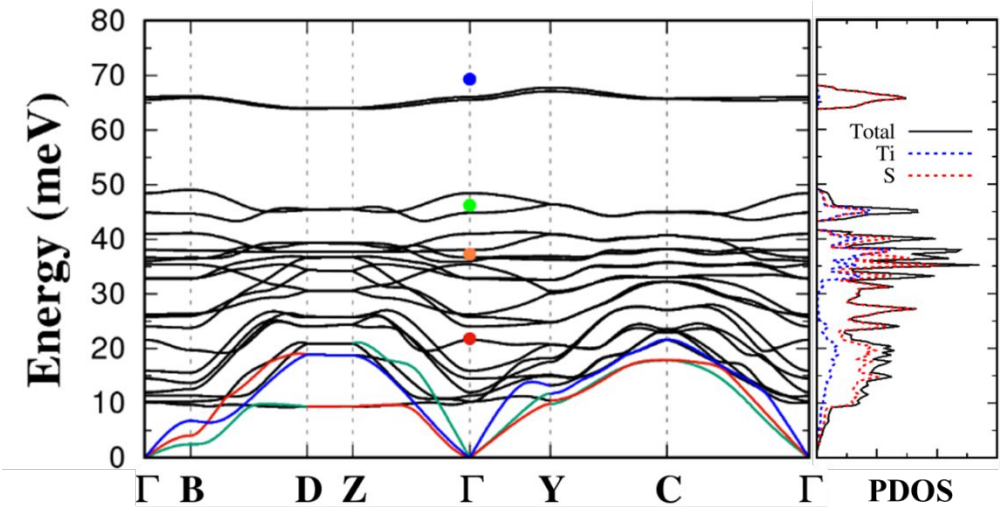

Figure S4. Phonon dispersion of TiS_3 calculated along its high-symmetry directions in the Brillouin zone and projected density of states (DOS) of Ti and S. The colored data points are

experimentally measured Raman peak energies.

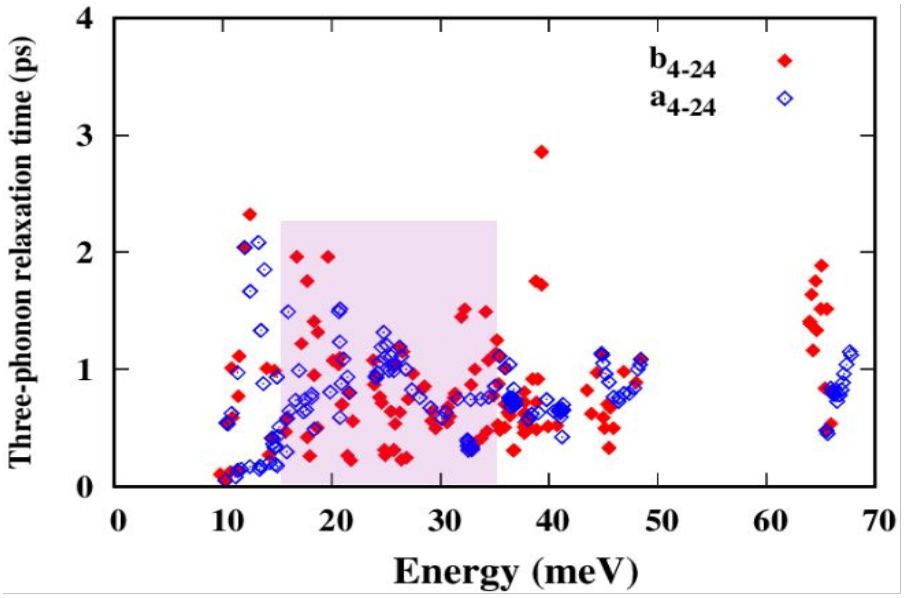

Figure S5. Relaxation time of all three-phonon processes as a function of optical phonon energy for TiS_3 at 300K. $a_{4\text{-}24}$ and $b_{4\text{-}24}$ indicates contribution from optical phonon branches along the a- and b-axis, respectively.

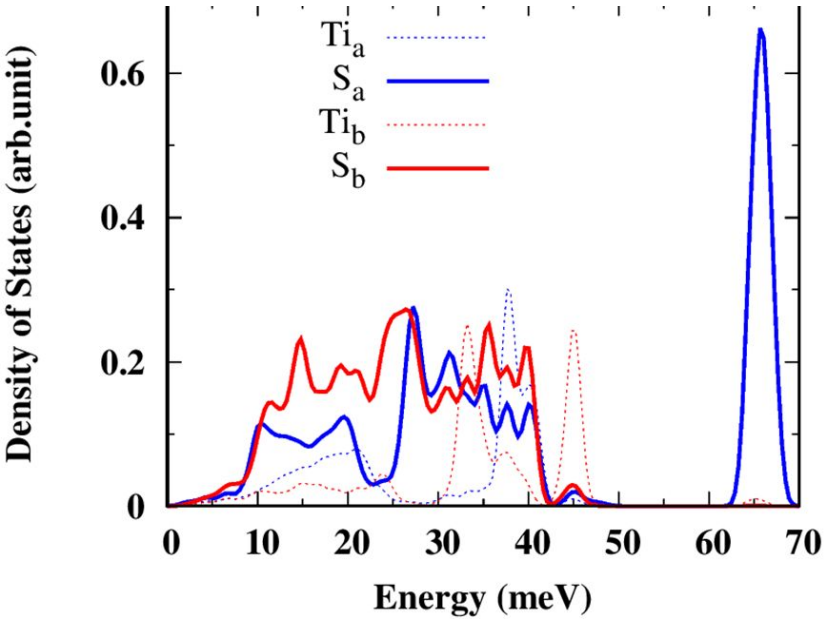

Figure S6. Partial phonon density of states (DOS) contributions from Ti and S atoms for phonons modes propagating along the a- and b-axis, respectively. The anisotropy of DOS from optical phonon modes between 15 - 30 meV proves that vibrations of S atoms for phonons propagating along b-axis contribute more to the DOS than that along a-axis.

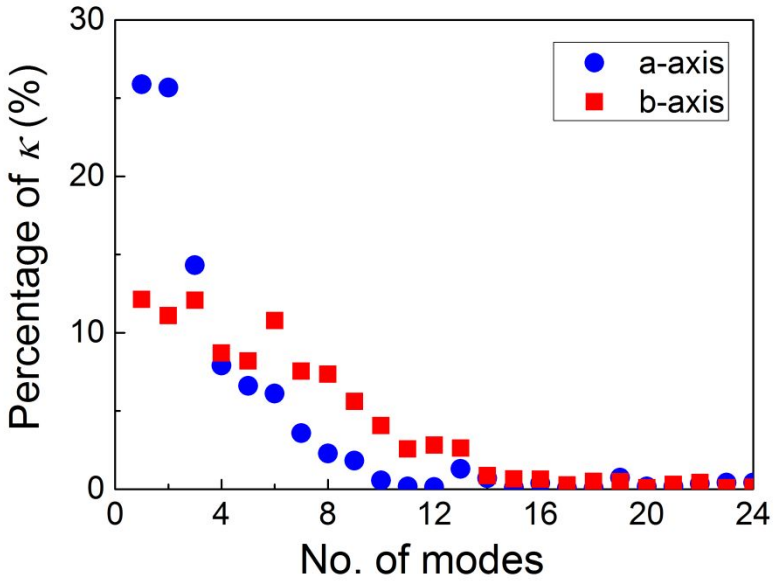

Figure S7. Percentage of contribution to κ from different phonon modes along its a- and b-axis, respectively. The optical phonon modes, No. 4-13 (~15 - 30 meV), show a significant anisotropy in contribution, where the modes along b-axis contribute more than that of a-axis.

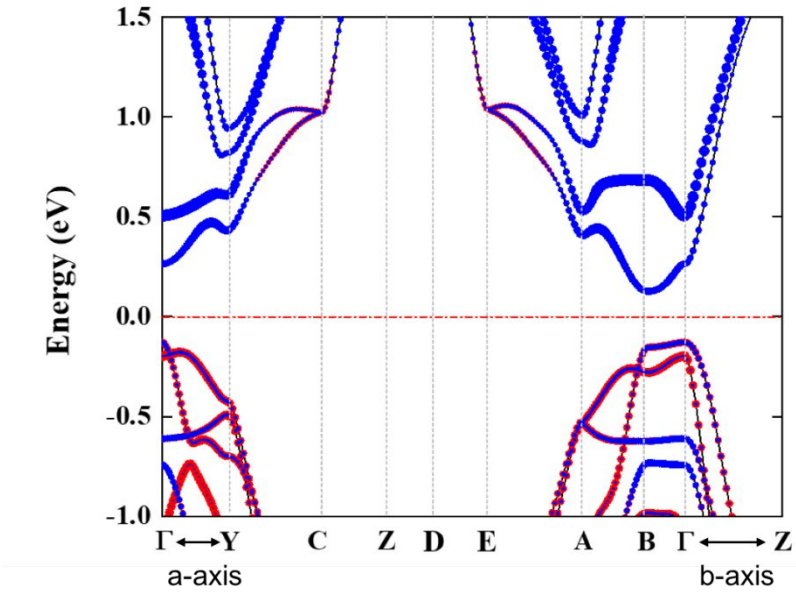

Figure S8. Electronic band structure of TiS_3. Blue and red dots indicate the contribution of Ti 3*d* and S 2*p* orbitals, respectively. The Ti 3*d* orbitals dominate the conduction band, dispersing mostly along the b-axis direction.

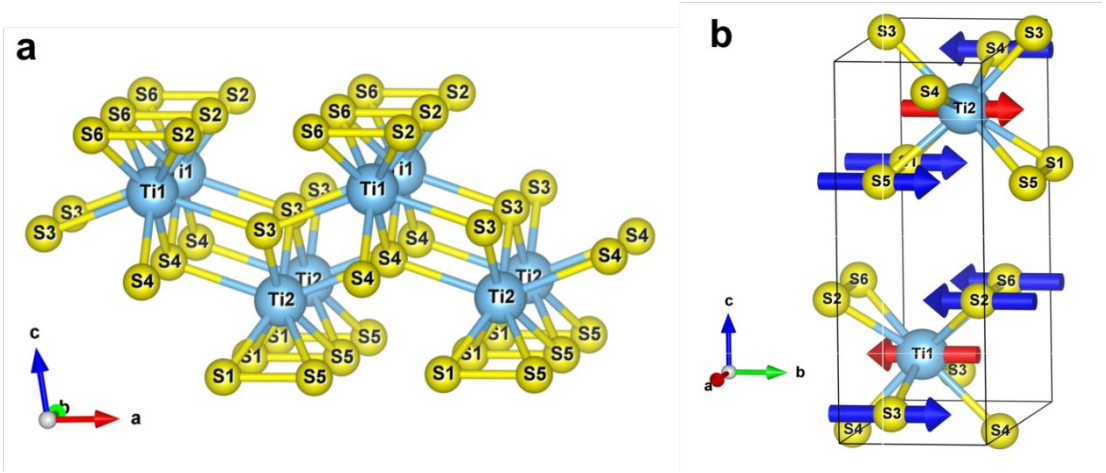

Figure S9. A crystal structure of TiS_3. (a) Ti1, S1, S3, and S5 atoms are equivalent to Ti2, S2, S4, and S6, respectively. (b) The arrows indicate the atomic displacement for Mode 8, the most dispersive optical vibration along the b-axis.

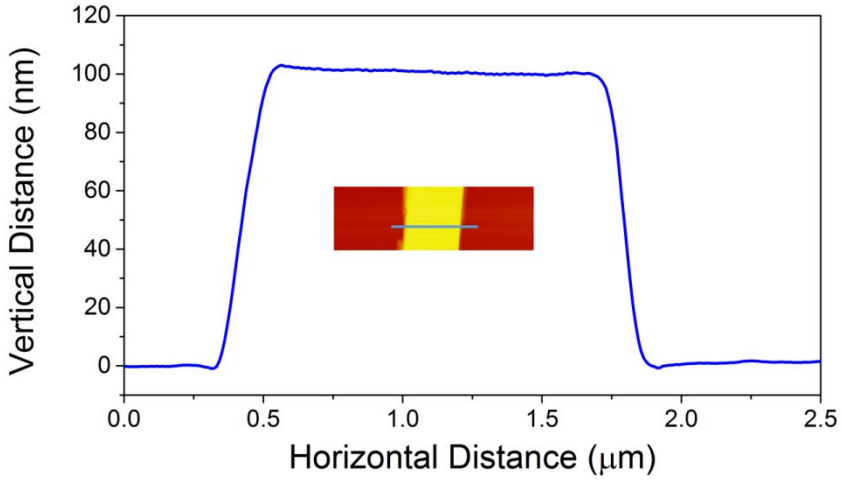

Figure S10. Height profile measured by AFM for a TiS_3 nanoribbon. Inset is an image of the nanoribbon and the line along which the height profile is taken.

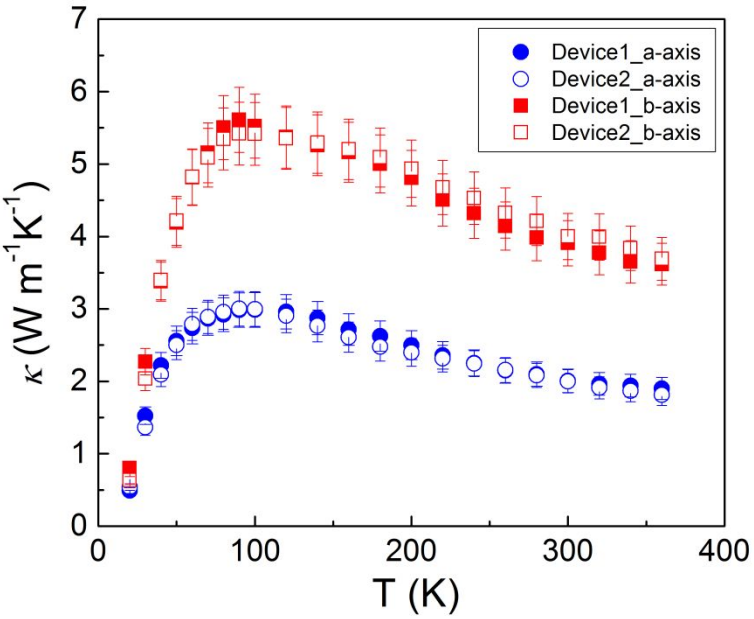

Figure S11. Thermal conductivity of TiS_3 nanoribbons along a- and b-axis plotted in linear scale.

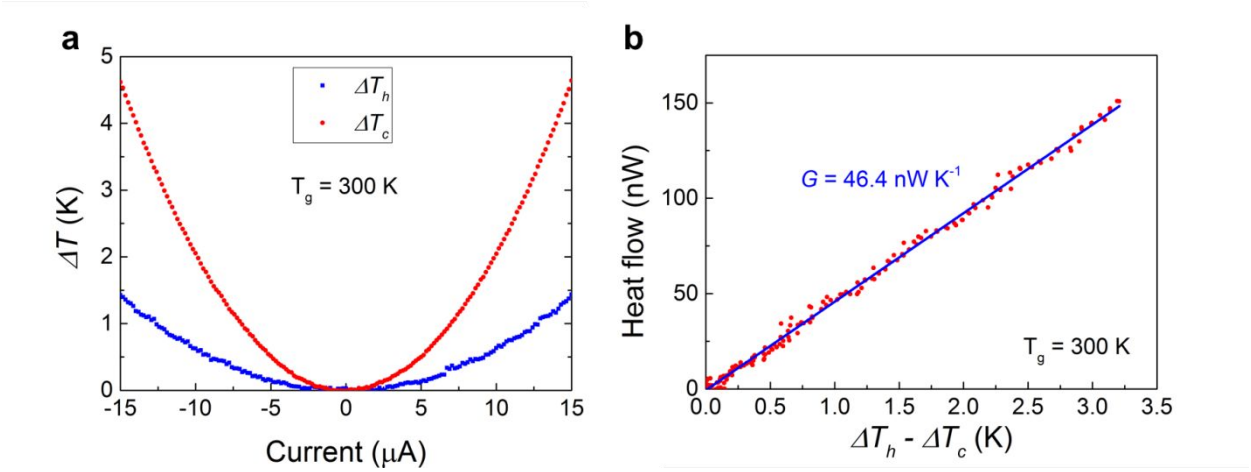

Figure S12. The measured thermal conductance at 300 K for Device2_b-axis. (a) A raising temperature of hot pad and cold pad as a function of the DC heating current. (b) Heat flow of nanoribbon as function of temperature difference between hot pad and cold pad.

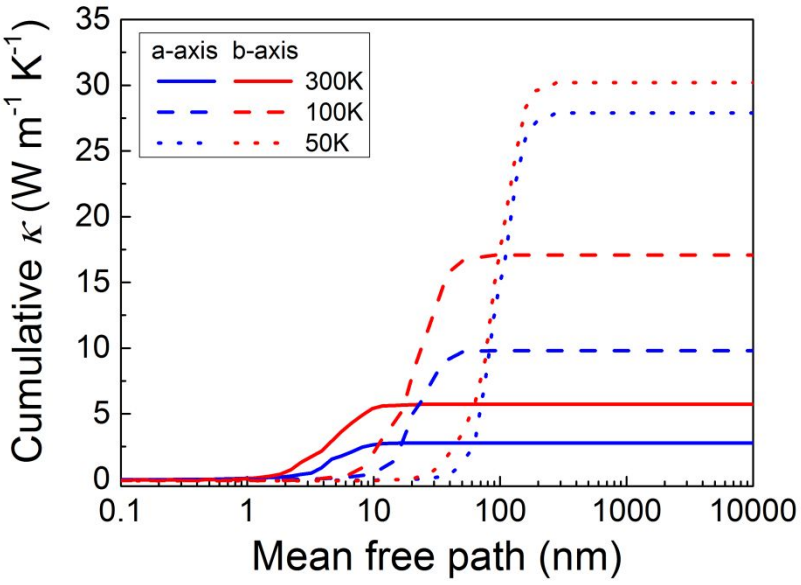

Figure S13. Cumulative thermal conductivity versus phonon mean free path along a- and b-axis at 300 K, 100 K, and 50 K, respectively.

		a-axis				b-axis			
		υ_{LA}	υ_{TA}	υ_{ZA}	υ_{ave_O}	υ_{LA}	υ_{TA}	υ_{ZA}	υ_{ave_O}
υ (km s^{-1})	Monolayer	5.43	3.01	0.88	-	6.16	2.31	1.11	-
	This work	5.71	3.00	2.73	0.49	5.94	3.45	2.97	1.02

Table S1. Group velocity of acoustic phonons (transverse (TA), longitudinal (LA) and out-of-plane (ZA)) and average velocity for the 21 optical phonons (υ_{ave_O}) near the Γ point, predicated by theoretical calculation (this work), compared to that of monolayer TiS_3 calculated by Zhang et al.[10] Group velocities (absolute value average for different q points) are averaged for $q/q_{max} < 0.2$.

		a-axis			b-axis		
κ, 300K (W m^{-1} K^{-1})	Monolayer, theoretical	10.2			17.9		
	This work, theoretical	acoustic	optical	total	acoustic	optical	total
		1.87	0.97	2.84	2.04	3.74	5.78
	This work, experimental	2.0			4.0		

Table S2. Theoretical and experimental lattice thermal conductivity at 300K (this work), compared to that of monolayer TiS_3 calculated by Zhang et al.[10]

Atoms		Ti1/Ti2	S1/S2	S3/S4	S5/S6
Born effective charge (e)	$(e^*)_{aa}$	1.92	-0.33	-1.51	-0.07
	$(e^*)_{bb}$	6.49	-1.57	-3.32	-1.69

Table S3. Calculated in-plane Born effective charge tensor for Ti and S in TiS_3, where the atoms are labeled in Figure S9a.